





This article may be downloaded for personal use only. Any other use requires prior permission of the author and AIP Publishing. This article appeared in *Journal of Applied Physics* 128, 055110 (2020); and may be found at: <https://doi.org/10.1063/5.0014883>

Copyright 2020 Author(s). This article is distributed under a Creative Commons Attribution 4.0 International (CC BY 4.0) License. <https://creativecommons.org/licenses/by/4.0/>

Phase transformation and magnetocaloric effect of Co-doped Mn–Ni–In melt-spun ribbons

Cite as: J. Appl. Phys. **128**, 055110 (2020); <https://doi.org/10.1063/5.0014883>

Submitted: 22 May 2020 . Accepted: 19 July 2020 . Published Online: 06 August 2020

Yiqiao Yang,  Zongbin Li,  César Fidel Sánchez-Valdés,  José Luis Sánchez Llamazares, Bo Yang, Yudong Zhang, Claude Esling, Xiang Zhao, and  Liang Zuo



View Online



Export Citation



CrossMark

ARTICLES YOU MAY BE INTERESTED IN

[Effects of interstitial C atoms on magnetostructural transformation and magnetocaloric effect in \$\text{MnNi}_{0.77}\text{Fe}_{0.23}\text{GeC}_x\$ compounds](#)

Journal of Applied Physics **128**, 023902 (2020); <https://doi.org/10.1063/1.5143608>

[Half-Heusler thermoelectric materials: NMR studies](#)

Journal of Applied Physics **128**, 055106 (2020); <https://doi.org/10.1063/5.0018260>

[Vanadium oxide coatings to self-regulate current sharing in high-temperature superconducting cables and magnets](#)

Journal of Applied Physics **128**, 055105 (2020); <https://doi.org/10.1063/5.0013783>



New

Your Qubits. Measured.

Meet the next generation of quantum analyzers

- Readout for up to 64 qubits
- Operation at up to 8.5 GHz, mixer-calibration-free
- Signal optimization with minimal latency

Find out more



Phase transformation and magnetocaloric effect of Co-doped Mn-Ni-In melt-spun ribbons

Cite as: J. Appl. Phys. 128, 055110 (2020); doi: 10.1063/5.0014883

Submitted: 22 May 2020 · Accepted: 19 July 2020 ·

Published Online: 6 August 2020



Yiqiao Yang,^{1,2} Zongbin Li,^{1,a)} César Fidel Sánchez-Valdés,³ José Luis Sánchez Llamazares,⁴ Bo Yang,¹ Yudong Zhang,⁵ Claude Esling,⁵ Xiang Zhao,^{1,a)} and Liang Zuo¹

AFFILIATIONS

¹Key Laboratory for Anisotropy and Texture of Materials (Ministry of Education), School of Material Science and Engineering, Northeastern University, Shenyang 110819, China

²Analytical and Testing Center, Northeastern University, Shenyang 110819, China

³División Multidisciplinaria, Ciudad Universitaria, Universidad Autónoma de Ciudad Juárez (UACJ), calle José de Jesús Macías Delgado # 18100, Ciudad Juárez 32579, Chihuahua, Mexico

⁴Instituto Potosino de Investigación Científica y Tecnológica A.C., Camino a la Presa San José 2055, Col. Lomas 4ª sección, San Luis Potosí 78216, Mexico

⁵Laboratoire d'Étude des Microstructures et de Mécanique des Matériaux (LEM3), CNRS UMR 7239, Université de Lorraine, 57045 Metz, France

^{a)}Authors to whom correspondence should be addressed: lizongbin@126.com and zhaox@mail.neu.edu.cn

ABSTRACT

Ribbon-shaped magnetocaloric materials are favorable to achieve high heat-transfer efficiencies due to their large specific surface area. In this work, $\text{Mn}_{50}\text{Ni}_{41-x}\text{In}_9\text{Co}_x$ ($0 \leq x \leq 4$) ribbons were prepared using a melt-spinning technique, and the corresponding phase transformation and magnetocaloric properties were studied. The large temperature gradient during melt-spinning caused the initial austenite in the ribbons to form typical columnar-shaped grains with a strong $(001)_A$ preferred orientation perpendicular to the ribbon plane. After cooling, the ribbons undergo martensitic transformation from cubic austenite to monoclinic eight-layered modulated (8 M) martensite. High angle annular dark field-scanning transmission electron microscopy observations indicate that martensite lattice modulation is inhomogeneous at atomic scales. Co substitution for Ni not only strongly influences the phase transformation temperatures but also greatly enhances ferromagnetic coupling. As a result, an enlarged magnetization difference across the martensitic transformation under a field change of 5 T in the $\text{Mn}_{50}\text{Ni}_{38}\text{In}_9\text{Co}_3$ ribbon induces a large magnetic entropy change up to $12.1 \text{ J kg}^{-1} \text{ K}^{-1}$ and a refrigeration capacity of 197 J kg^{-1} around room temperature. In addition, a wide operational temperature region up to 31 K is obtained in the $\text{Mn}_{50}\text{Ni}_{37}\text{In}_9\text{Co}_4$ ribbon due to the enhanced sensitivity of the transformation temperature shift under a magnetic field.

Published under license by AIP Publishing. <https://doi.org/10.1063/5.0014883>

I. INTRODUCTION

Heusler type Ni-Mn-X (X=In, Sn, and Sb) based meta-magnetic shape memory alloys with a first-order magnetostructural transformation from ferromagnetic austenite to weak magnetic martensite have generated considerable attention in recent years.¹ The significant magnetization difference between austenite and martensite allows the inverse martensitic transformation to be induced from magnetic fields,² giving rise to various functional behaviors such as the magnetic shape memory effect,²⁻⁶ the magnetoresistance effect,⁷⁻⁹ and the magnetocaloric effect (MCE).¹⁰⁻¹⁶ Therefore, these

alloys are conceived as potential candidates for actuators, sensors, and magnetic refrigeration applications.

The magnetocaloric effect (MCE) is the intrinsic thermal response of magnetic materials with the application or removal of an external magnetic field, which can be evaluated based on the isothermal magnetic entropy change (ΔS_M) or adiabatic temperature change (ΔT_{ad}). In general, the MCE is strongly related to the magnetization difference ΔM across the phase transition with a higher ΔM allowing for a more remarkable magnetocaloric response. As the magnetization of Ni-Mn-based alloys results primarily from contributions of

Mn,¹⁵ proper tuning on the Mn content can be exploited to enlarge ΔM between the austenite and martensite phases. Therefore, the exploration of high-Mn content Mn–Ni-based alloys is of particular interest, which may not only enlarge the composition range but may allow developing high-performance magnetocaloric materials. It has been confirmed that in some high-Mn content Mn–Ni-based alloys, there is a magnetostructural transformation from ferromagnetic austenite to weak magnetic martensite,¹⁷ and a significant MCE has been achieved.^{18–22} It is noted that candidate magnetocaloric materials for potential magnetic refrigeration should possess not only a large MCE but also a wide operational temperature range. However, the relatively low Curie temperature of austenite (T_C) in the high-Mn content Mn–Ni-based alloys^{19–24} (around or even below 300 K) imposes a strong constraint on the temperature range of magnetostructural transformation and the corresponding MCE. This is because the occurrence of magnetostructural transformations from ferromagnetic austenite to weak magnetic martensite requires T_C to be higher than the martensitic transformation temperature (T_M). In such challenges, introducing a fourth element could be an efficient way to manipulate the T_C and its corresponding temperature range of magnetostructural transformation.

It is noted that heat-transfer is of great importance for potential magnetic refrigeration applications. Magnetocaloric materials with large specific surface areas (e.g., sheets and ribbons) are expected to present high heat-transfer efficiencies. However, the intrinsic brittleness of bulk Ni–Mn-based Heusler alloys makes them more difficult to process into thin sheets. In particular, high-Mn contents may further increase the brittleness of bulk alloys. Thus, the melt-spinning technique is conceived as an ideal method to produce ribbons through rapid solidification from the liquid metal. Recently, some specific Heusler alloys with highly homogeneous compositions have been successfully prepared via melt-spinning.^{21,22,24–26} In addition, ribbon-shaped samples help minimize the demagnetization effect during magnetization/demagnetization cycles. The demagnetization effect could become negligible due to the large length-to-thickness ratio when a magnetic field is applied along the longitudinal direction.

It is noted that Co doping not only effectively influences the magnetic and structural transformation temperatures but also enhances ferromagnetic coupling.^{2,11,27,28} Therefore, Co was introduced in this work to replace Ni to tune the magnetostructural transformation parameters and improve the magnetocaloric properties. A series of high-Mn content $\text{Mn}_{50}\text{Ni}_{41-x}\text{In}_9\text{Co}_x$ ($0 \leq x \leq 4$) ribbons were prepared using the melt-spinning technique. The magnetostructural transformation and related magnetocaloric properties of the ribbons were studied. It is shown that the ribbons underwent martensitic transformation from cubic austenite to monoclinic eight-layered modulated (8 M) martensite. The high angle annular dark field-scanning transmission electron microscopy (HAADF-STEM) observations indicate that the lattice modulation of martensite is inhomogeneous at the atomic scale. The introduction of Co converted the martensitic transformation from paramagnetic to meta-magnetic, which resulted in significant increases in the magnetization difference ΔM across magnetostructural transformation. Consequently, a large magnetic entropy change ΔS_M of $12.1 \text{ J kg}^{-1} \text{ K}^{-1}$ and refrigeration capacity RC up to 197 J kg^{-1} were obtained in the $\text{Mn}_{50}\text{Ni}_{38}\text{In}_9\text{Co}_3$ melt-spun ribbon

TABLE I. Composition and e/a ratio for the $\text{Mn}_{50}\text{Ni}_{41-x}\text{In}_9\text{Co}_x$ ($0 \leq x \leq 4$) ribbons.

Target composition	Actual composition (at. %)				e/a
	Mn	Ni	In	Co	
$\text{Mn}_{50}\text{Ni}_{41}\text{In}_9\text{Co}_0$	50.1	40.9	9.0	0	7.870
$\text{Mn}_{50}\text{Ni}_{40}\text{In}_9\text{Co}_1$	50.2	39.9	8.9	1.0	7.867
$\text{Mn}_{50}\text{Ni}_{39}\text{In}_9\text{Co}_2$	50.2	39.1	8.7	2.0	7.863
$\text{Mn}_{50}\text{Ni}_{38}\text{In}_9\text{Co}_3$	50.1	38.0	9.0	2.9	7.838
$\text{Mn}_{50}\text{Ni}_{37}\text{In}_9\text{Co}_4$	50.2	36.9	9.0	3.9	7.825

under a field change of 5 T. Moreover, the enhanced sensitivity of the transformation shift under a magnetic field provides a wide operational temperature region of 31 K in the $\text{Mn}_{50}\text{Ni}_{37}\text{In}_9\text{Co}_4$ ribbon.

II. EXPERIMENTAL METHODS

Bulk polycrystalline alloys with a nominal composition of $\text{Mn}_{50}\text{Ni}_{41-x}\text{In}_9\text{Co}_x$ ($0 \leq x \leq 4$, at. %) were prepared via arc-melting using high purity metal elements under the protection of an argon atmosphere. To achieve good composition homogeneity, the as-cast alloys were remelted several times. The ribbons were prepared in a single copper roller melt-spinning device at a rotation speed of 20 ms^{-1} under an argon atmosphere using the as-cast alloy as the master material. The ribbon composition was verified using x-ray wave dispersive spectrometry (WDS). As shown in Table I, the actual compositions of the studied ribbons were quite close to the target cases. The characteristic temperatures for the forward and inverse martensitic transformation (M_s , M_f , A_s , and A_f) were measured using differential scanning calorimetry (DSC) with heating and cooling rates of 10 K min^{-1} . The room temperature crystal structure was determined via x-ray diffraction (XRD) with Cu-K α radiation and selected area electronic diffraction (SAED). The pole figures were measured with XRD at room temperature on the ribbon plane. The microstructural characterization was performed with a JEOL JSM-7001F scanning electron microscope (SEM) and a JEOL JEM-ARM200F transmission electron microscope (TEM). The magnetization measurements were performed in a physical property measuring system (PPMS-9 T, Quantum Design), where the magnetic field was applied along the longitudinal (rolling) direction of the ribbons to minimize the influence of demagnetization.

III. RESULTS AND DISCUSSION

A. Crystal structure and microstructural features

The XRD measurements were performed at room temperature on the ribbon plane to detect the phase constitution of the $\text{Mn}_{50}\text{Ni}_{41-x}\text{In}_9\text{Co}_x$ ($0 \leq x \leq 4$) ribbons. It is shown that the $\text{Mn}_{50}\text{Ni}_{41}\text{In}_9$ and $\text{Mn}_{50}\text{Ni}_{40}\text{In}_9\text{Co}_1$ ribbons possessed single martensite at room temperature. With an increased Co content, the room temperature phase gradually evolved into austenite, i.e., a mixture of austenite and martensite for the $\text{Mn}_{50}\text{Ni}_{39}\text{In}_9\text{Co}_2$ ribbon and single austenite for the $\text{Mn}_{50}\text{Ni}_{38}\text{In}_9\text{Co}_3$ and $\text{Mn}_{50}\text{Ni}_{37}\text{In}_9\text{Co}_4$ ribbons. This indicates that Co substitution for Ni results in a decreased martensitic transformation temperature. Typical room-temperature XRD

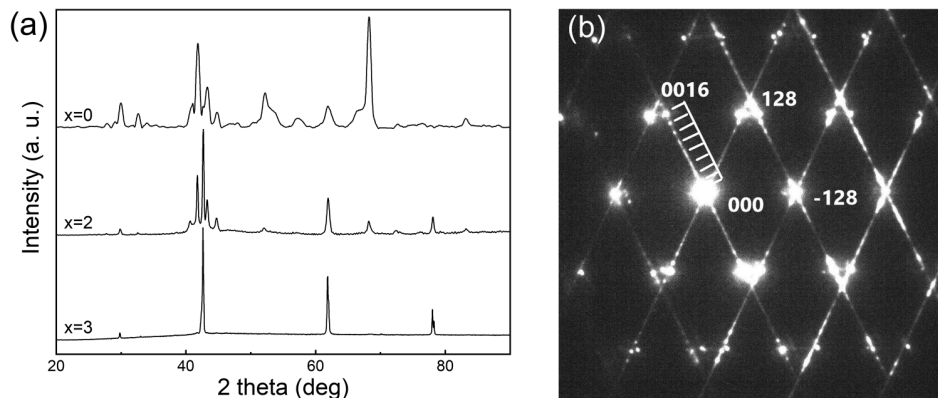


FIG. 1. (a) Typical room-temperature XRD patterns for $\text{Mn}_{50}\text{Ni}_{41-x}\text{In}_9\text{Co}_2$ ribbons and (b) the selected area electronic diffraction (SAED) pattern for martensite along the $\langle 210 \rangle_M$ direction.

patterns for the $\text{Mn}_{50}\text{Ni}_{41}\text{In}_9$, $\text{Mn}_{50}\text{Ni}_{39}\text{In}_9\text{Co}_2$, and $\text{Mn}_{50}\text{Ni}_{38}\text{In}_9\text{Co}_3$ ribbons are shown in Fig. 1(a). Several diffraction peaks for the martensitic phase in the 2θ range of 40° – 45° are seen for the $\text{Mn}_{50}\text{Ni}_{41}\text{In}_9$ and $\text{Mn}_{50}\text{Ni}_{39}\text{In}_9\text{Co}_2$ ribbons, which could indicate lattice modulation for martensite. The SAED measurements were performed to gain greater insight into the period of lattice modulation. A typical SAED pattern along the $\langle 210 \rangle_M$ direction of martensite as acquired for the $\text{Mn}_{50}\text{Ni}_{39}\text{In}_9\text{Co}_2$ ribbon is shown in Fig. 1(b). Seven satellite spots are located between the two main diffraction spots, indicating a monoclinic 8 M-type crystal structure in the ribbons.²⁹ In addition, it is found that the satellite spots exhibit the characteristics of elongation and even dispersion.

Figures 2(a)–2(c) show backscattered electron (BSE) images of the ribbon plane for the $\text{Mn}_{50}\text{Ni}_{40}\text{In}_9\text{Co}_1$, $\text{Mn}_{50}\text{Ni}_{39}\text{In}_9\text{Co}_2$, and

$\text{Mn}_{50}\text{Ni}_{36}\text{In}_9\text{Co}_4$ ribbons, respectively, which exhibit the microstructure of single martensite, a mixture of martensite and austenite, and single austenite. The austenite morphology exhibits equiaxed grains and the martensite is in a plate shape within the initial austenite grains. The ultra-high cooling rate of the melt-spinning process significantly reduces the grain size of the initial austenite ($\sim 10\ \mu\text{m}$), which is much smaller than for bulk alloys.²⁸

Figure 2(d) shows a secondary electron image taken from the cross section of the $\text{Mn}_{50}\text{Ni}_{36}\text{In}_9\text{Co}_4$ ribbon. The initial austenite grains are characterized as columnar shaped with the longer axes perpendicular to the ribbon plane. Such a microstructural feature is attributed to the specific temperature gradient during the melt-spinning process.³⁰ In addition, it is found that the grain size at the wheel surface side is much smaller than at the free surface side,

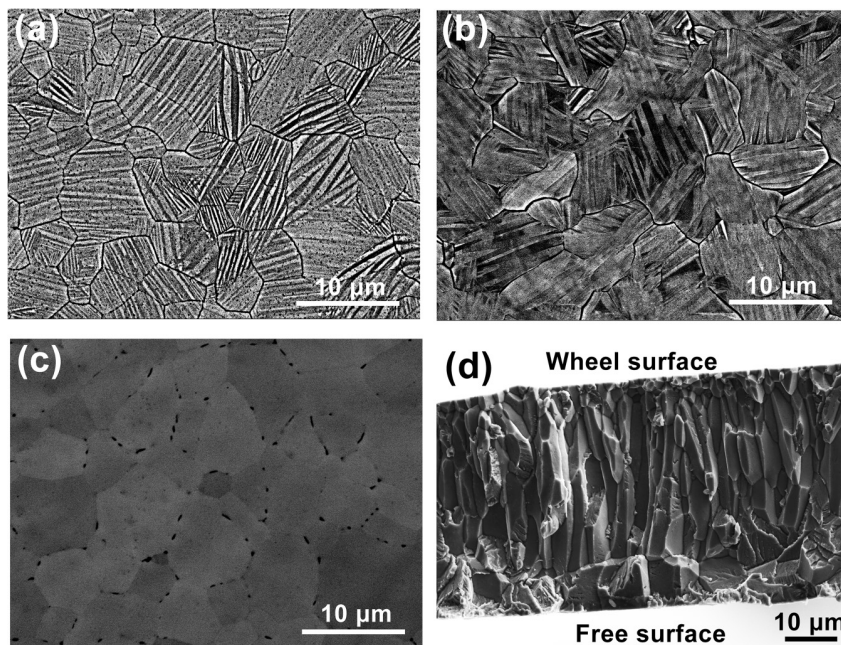


FIG. 2. (a) BSE image of the ribbon plane for (a) $\text{Mn}_{50}\text{Ni}_{40}\text{In}_9\text{Co}_1$, (b) $\text{Mn}_{50}\text{Ni}_{39}\text{In}_9\text{Co}_2$, and (c) $\text{Mn}_{50}\text{Ni}_{37}\text{In}_9\text{Co}_4$ ribbons and (d) secondary electron image of cross section of the $\text{Mn}_{50}\text{Ni}_{37}\text{In}_9\text{Co}_4$ ribbon.

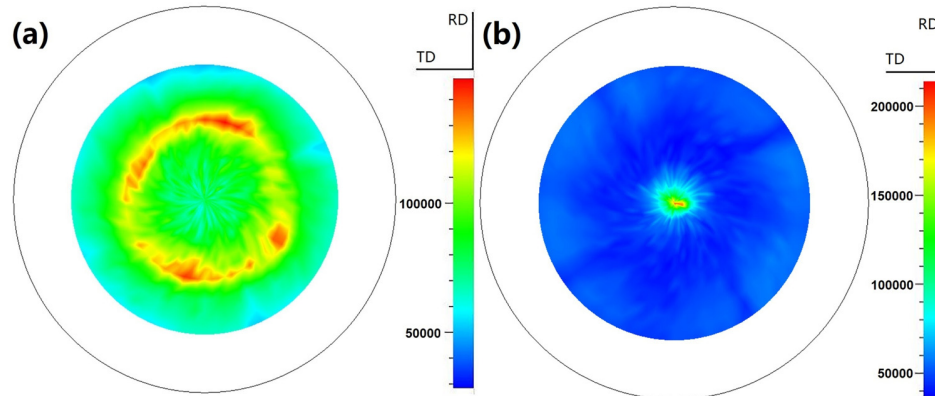


FIG. 3. Pole figures for the $\text{Mn}_{50}\text{Ni}_{37}\text{In}_9\text{Co}_4$ ribbon measured on the ribbon plane with XRD for (a) $\{220\}_A$ and (b) $\{400\}_A$.

which is consistent with previous observations.³⁰ This effect is attributed to the relatively higher cooling rate at the wheel surface side due to its direct contact with the copper wheel.³⁰

Figures 3(a) and 3(b) show the $\{220\}_A$ and $\{400\}_A$ pole figures, respectively, of austenite for the $\text{Mn}_{50}\text{Ni}_{37}\text{In}_9\text{Co}_4$ ribbon measured at the ribbon plane using room-temperature XRD. The $\{220\}_A$ poles are located primarily at the polar angle of $\sim 40^\circ$, and the $\{400\}_A$ poles are at the center in the corresponding pole figures. Therefore, it is inferred that austenite possesses a strong preferred orientation with $\langle 001 \rangle_A$ perpendicular to the ribbon plane.³¹ This microstructural feature is ascribed to the thermal gradient during the melt-spinning process.^{30,31}

Figure 4(a) presents a TEM bright-field image of the 8 M martensite plates for the $\text{Mn}_{50}\text{Ni}_{39}\text{In}_9\text{Co}_2$ ribbon. The substructure of the martensite plates is characterized as stacking faults. Locally, four types of martensite variants [represented as A, B, C, and D in Fig. 4(a)] are alternately distributed, which agree with the modulated martensite having the monoclinic structure in Ni-Mn-Ga alloys.^{32,33} Scanning transmission electron microscopy (STEM) observations were performed to gain deeper insight into the

internal microstructural feature of martensite. Figure 4(b) shows a typical HAADF-STEM image for 8 M martensite along the $\langle 010 \rangle_M$ axis. The stacking periodicity for the 8 M martensite is inhomogeneous as each stacking periodicity contains different atomic layers, as indicated in Fig. 4(b). This may cause irregular spacing of the satellite spots between two main spots and result in their elongation [Fig. 1(b)].

B. Phase transformation

Figure 5(a) shows the DSC curves for the $\text{Mn}_{50}\text{Ni}_{41-x}\text{In}_9\text{Co}_x$ melt-spun ribbons. The appearance of exothermic and endothermic peaks for the cooling and heating stages indicates the occurrence of forward and inverse martensitic transformations, respectively. The tangent method was used to find the start and finish temperatures (M_s , M_f , A_s , and A_f) for the forward and inverse transformations with their compositional dependence presented in Fig. 5(b). The martensitic transformation temperatures gradually decrease with the Co content. As indicated in Table I, Co substitution for Ni gradually decreases the valence electron concentration e/a . Thus,

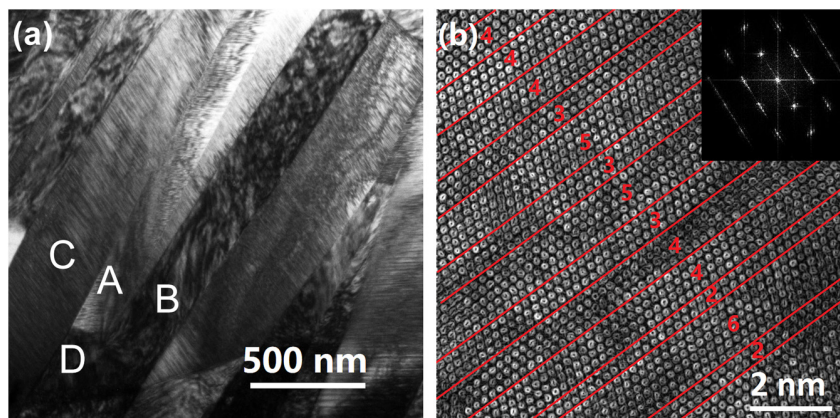


FIG. 4. (a) TEM bright-field image of 8M martensite for the $\text{Mn}_{50}\text{Ni}_{39}\text{In}_9\text{Co}_2$ ribbon and (b) HAADF-STEM image of 8M martensite along the $\langle 010 \rangle_M$ axis. The inset in (b) shows the corresponding fast Fourier Transformation (FFT) pattern.

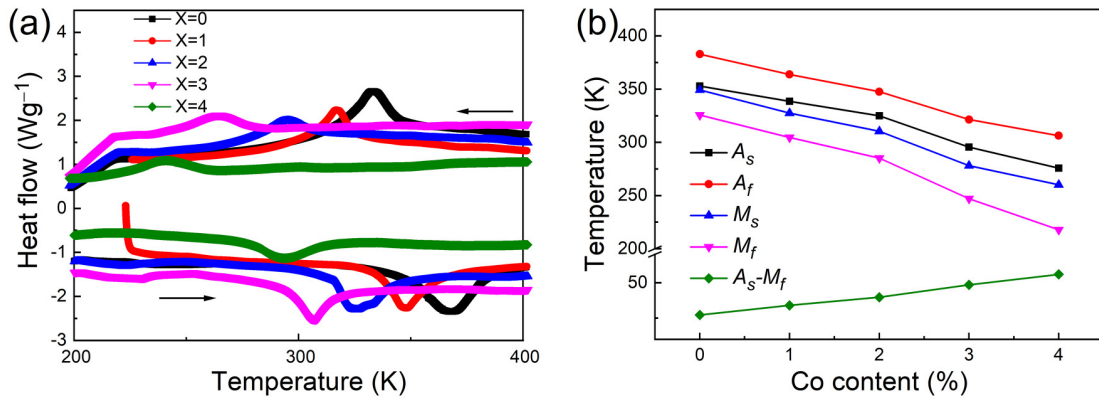


FIG. 5. (a) DSC curves for Mn₅₀Ni_{41-x}In₉Co_x (x=0-4) ribbons, and (b) the compositional dependence of the martensitic transformation temperatures and thermal hysteresis (A_s - M_f).

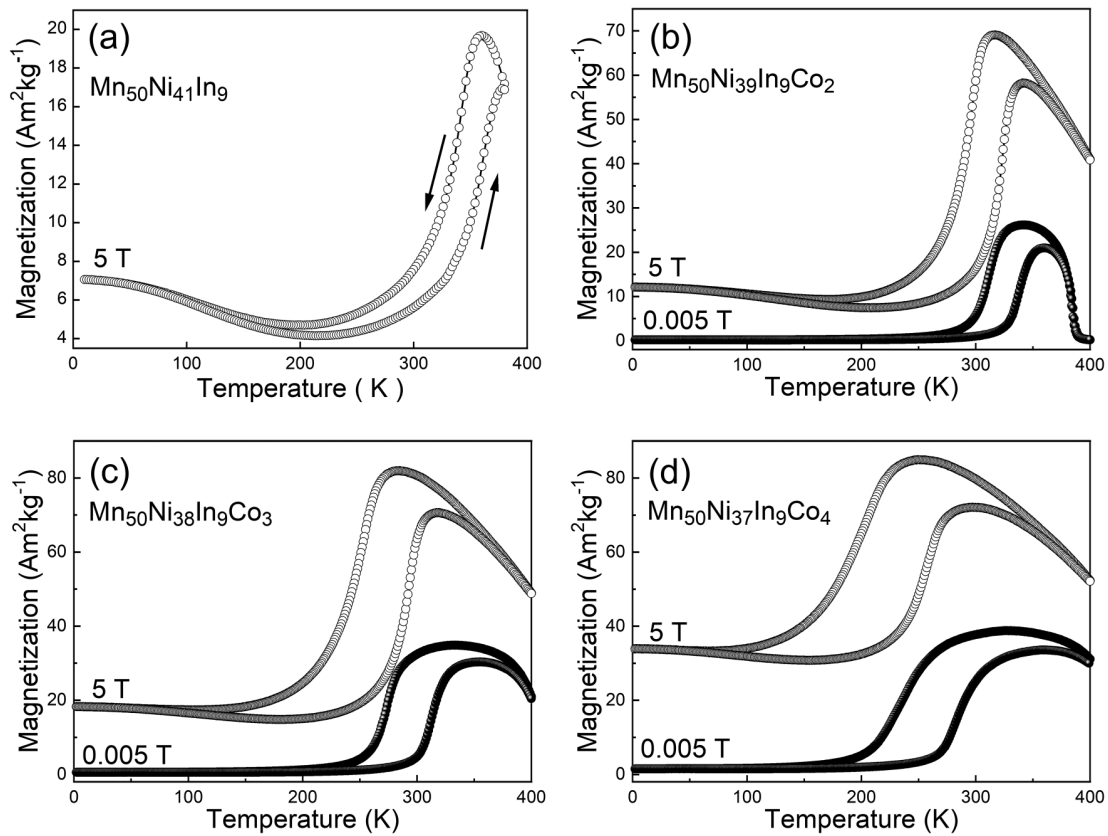


FIG. 6. *M-T* curves for the (a) Mn₅₀Ni₄₁In₉, (b) Mn₅₀Ni₃₉In₉Co₂, (c) Mn₅₀Ni₃₈In₉Co₃, and (d) Mn₅₀Ni₃₇In₉Co₄ ribbons.

this gradual decrease in the martensitic transformation temperature is attributed to a reduced e/a .¹¹ In addition, Co substitution for Ni can also exert a certain influence on the thermal hysteresis. As indicated in Fig. 5(b), the thermal hysteresis, determined as $A_s - M_f$, gradually increases with the Co content, which is consistent with previous results.¹¹

The temperature dependence of magnetization (M - T curves) was measured to analyze changes associated with martensitic transformation. The results show that martensitic transformation for the $Mn_{50}Ni_{41}In_9$ and $Mn_{50}Ni_{40}In_9Co_1$ ribbons occurred from the paramagnetic austenite to the weak magnetic martensite. Typical M - T curves for the $Mn_{50}Ni_{41}In_9$ ribbon under a magnetic field of 5 T are shown in Fig. 6(a). The magnetization difference ΔM across martensitic transformation in the $Mn_{50}Ni_{41}In_9$ ribbon is relatively low at $\Delta M = 16 A m^2 kg^{-1}$.

Figures 6(b)–6(d) present the M - T curves for the $Mn_{50}Ni_{39}In_9Co_2$, $Mn_{50}Ni_{38}In_9Co_3$, and $Mn_{50}Ni_{37}In_9Co_4$ ribbons, respectively, under magnetic fields of 0.005 T and 5 T. For the $Mn_{50}Ni_{39}In_9Co_2$ ribbon, T_C is determined as 383 K from the M - T curves at a field of 0.005 T. However, for the $Mn_{50}Ni_{38}In_9Co_3$ and

$Mn_{50}Ni_{37}In_9Co_4$ ribbons, T_C was not detected until 400 K. Thus, the paramagnetic to ferromagnetic transition of austenite may occur at temperatures above 400 K as Co substitution for Ni results in an increased T_C .¹¹ Compared to the $Mn_{50}Ni_{41}In_9$ ribbon, the magnetization difference ΔM associated with martensitic transformation in the $Mn_{50}Ni_{39}In_9Co_2$, $Mn_{50}Ni_{38}In_9Co_3$, and $Mn_{50}Ni_{37}In_9Co_4$ ribbons was greatly enhanced. Taking the $Mn_{50}Ni_{38}In_9Co_3$ ribbon as an example, a large ΔM up to $68 A m^2 kg^{-1}$ associated with martensitic transformation was achieved, indicating strong magnetostructural coupling. Moreover, the martensitic transformation shifted to the lower temperature region after the application of a magnetic field of 5 T, which indicates that the inverse martensitic transformation can be induced from magnetic fields. For the $Mn_{50}Ni_{39}In_9Co_2$, $Mn_{50}Ni_{38}In_9Co_3$, and $Mn_{50}Ni_{37}In_9Co_4$ ribbons, A_s was reduced by 26, 30, and 37 K under a magnetic field of 5 T, respectively, with corresponding reduction rates of 5.2, 6, and $7.4 K T^{-1}$. Thus, Co doping results in large magnetic field-induced transformation temperature shifts.

The reduction in the transformation temperature (ΔT) induced from magnetic fields is described using the Clausius–

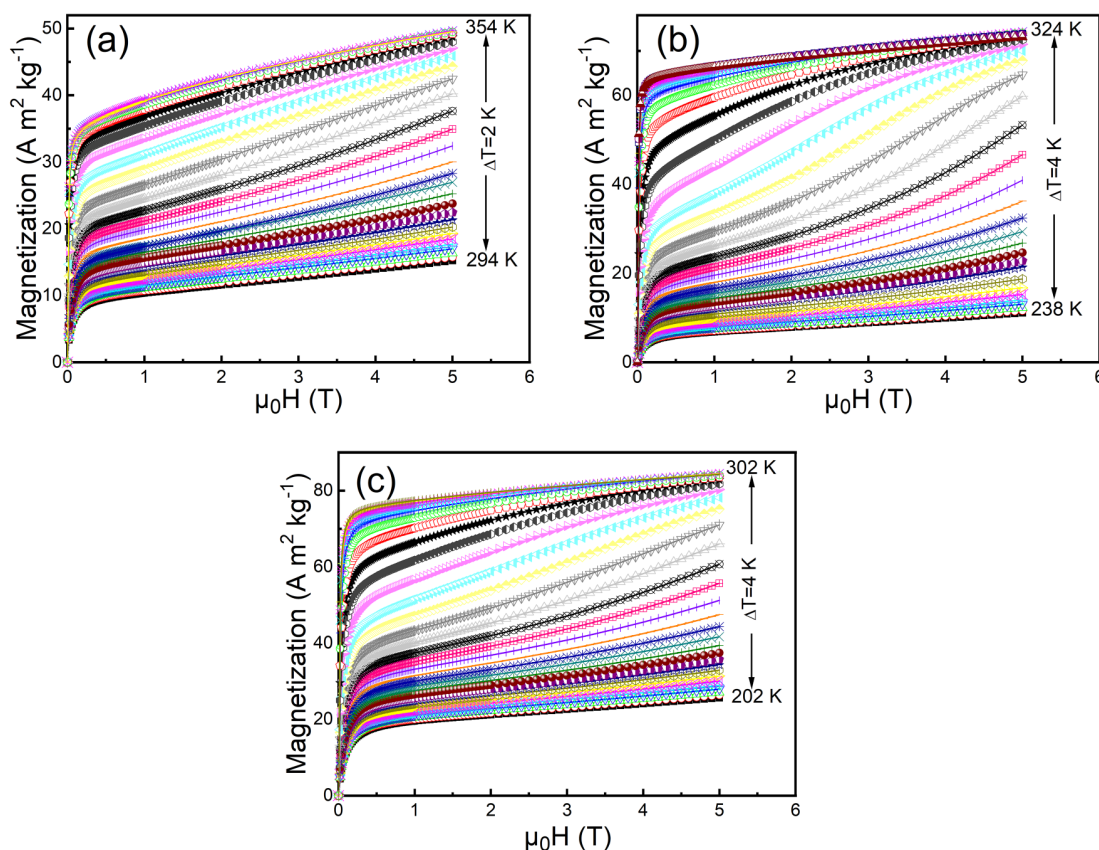


FIG. 7. Isothermal magnetization curves across the inverse martensitic transformation for the (a) $Mn_{50}Ni_{39}In_9Co_2$, (b) $Mn_{50}Ni_{38}In_9Co_3$, and (c) $Mn_{50}Ni_{37}In_9Co_4$ melt-spun ribbons with a maximum magnetic field of 5 T.

Clapeyron relation as $\Delta T/\mu_0\Delta H = \Delta M/\Delta S$, where ΔS and ΔM represent changes in entropy and magnetization across transformation, respectively. For the $\text{Mn}_{50}\text{Ni}_{38}\text{In}_9\text{Co}_3$ ribbon, ΔS was determined as $12.4 \text{ J kg}^{-1} \text{ K}^{-1}$ through DSC measurements. Thus, ΔT induced from applying a magnetic field of 5 T is estimated as 27.4 K based on the Clausius–Clapeyron relation, which is close to the experimentally observed temperature shift of 30 K.

C. Magnetocaloric properties

The above thermo-magnetic measurements suggest that the $\text{Mn}_{50}\text{Ni}_{39}\text{In}_9\text{Co}_2$, $\text{Mn}_{50}\text{Ni}_{38}\text{In}_9\text{Co}_3$, and $\text{Mn}_{50}\text{Ni}_{37}\text{In}_9\text{Co}_4$ ribbons possess relatively high ΔM across martensitic transformation, which indicates a large expected MCE. To evaluate the magnetocaloric properties, sets of isothermal magnetization (M - H) curves across the inverse martensitic transformation were measured with a maximum field of 5 T to determine the entropy change (ΔS_M) induced from the magnetic field, as shown Fig. 7. To avoid overestimation of ΔS_M , the M - H curves were measured using a loop

method: before the M - H measurements at each testing temperature, the sample was first cooled to low temperature under a zero field to achieve the full martensite state. The sample was then heated to the testing temperature under a zero field.

The M - H curves allow calculating the magnetic field-induced entropy change ΔS_M across inverse martensitic transformation using Maxwell's relation. Figures 8(a)–8(c) show the temperature dependence of ΔS_M under magnetic field variations from 1 to 5 T for the $\text{Mn}_{50}\text{Ni}_{39}\text{In}_9\text{Co}_2$, $\text{Mn}_{50}\text{Ni}_{38}\text{In}_9\text{Co}_3$, and $\text{Mn}_{50}\text{Ni}_{37}\text{In}_9\text{Co}_4$ ribbons, respectively. The ribbons exhibit large inverse MCE around room temperature, which is consistent with the decreased martensitic transformation temperatures at larger magnetic fields. It is noted that the field-induced inverse martensitic transformation causes the ΔS_M peaks to gradually shift to lower temperatures for larger magnetic fields. Under a field change $\mu_0\Delta H$ of 5 T, the maximum ΔS_M for the $\text{Mn}_{50}\text{Ni}_{39}\text{In}_9\text{Co}_2$, $\text{Mn}_{50}\text{Ni}_{38}\text{In}_9\text{Co}_3$, and $\text{Mn}_{50}\text{Ni}_{37}\text{In}_9\text{Co}_4$ ribbons was 5.7, 12.1, and $7.5 \text{ J kg}^{-1} \text{ K}^{-1}$, respectively. Compared with the ternary $\text{Mn}_{50}\text{Ni}_{40.5}\text{In}_{9.5}$ ribbon ($\Delta S_M = 6.1 \text{ J kg}^{-1} \text{ K}^{-1}$),²⁹ the ΔS_M values for the Co-doped ribbons

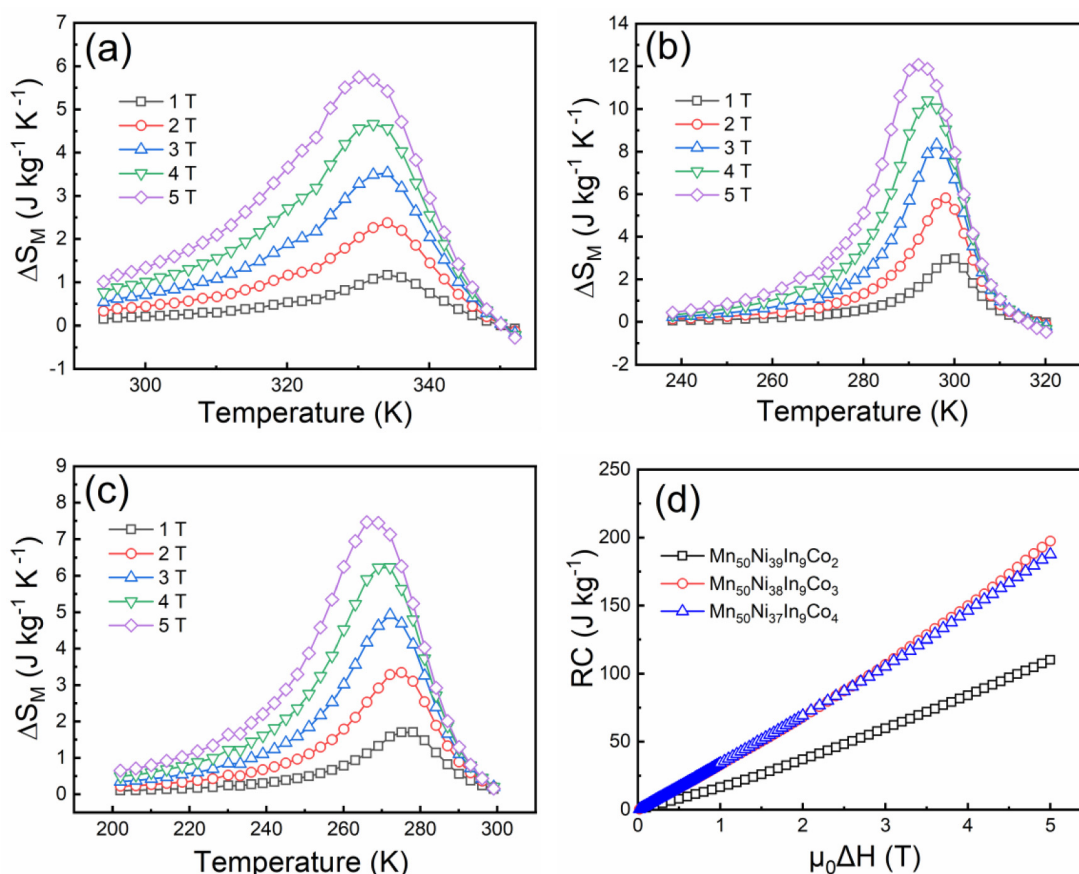


FIG. 8. Temperature dependence of ΔS_M under various magnetic field changes for the (a) $\text{Mn}_{50}\text{Ni}_{39}\text{In}_9\text{Co}_2$, (b) $\text{Mn}_{50}\text{Ni}_{38}\text{In}_9\text{Co}_3$, and (c) $\text{Mn}_{50}\text{Ni}_{37}\text{In}_9\text{Co}_4$ ribbon and the (d) field dependences of RC.

are greatly improved. Moreover, the maximum ΔS_M values are comparable with those of bulk $\text{Mn}_{50}\text{Ni}_{40}\text{Sn}_{10}$ ($\Delta S_M = 8.6 \text{ J kg}^{-1} \text{ K}^{-1}$),³⁴ $\text{Mn}_{50}\text{Ni}_{39}\text{Co}_1\text{Sn}_{10}$ ($\Delta S_M = 10.5 \text{ J kg}^{-1} \text{ K}^{-1}$),³⁴ $\text{Ni}_{50}\text{Mn}_{34.8}\text{In}_{15.2}$ ($\Delta S_M = 13 \text{ J kg}^{-1} \text{ K}^{-1}$),³⁵ $\text{Ni}_{49.0}\text{Mn}_{35.9}\text{In}_{7.1}\text{Sb}_{8.0}$ ($\Delta S_M = 10 \text{ J kg}^{-1} \text{ K}^{-1}$),³⁶ $\text{Ni}_{50}\text{Mn}_{35}\text{In}_{14.25}\text{B}_{0.75}$ ($\Delta S_M = 10 \text{ J kg}^{-1} \text{ K}^{-1}$),³⁷ $\text{Ni}_{49.8}\text{Co}_{1.2}\text{Mn}_{33.5}\text{In}_{15.5}$ ($\Delta S_M = 14.6 \text{ J kg}^{-1} \text{ K}^{-1}$),³⁸ $\text{Ni}_{46}\text{Co}_4\text{Mn}_{38}\text{Sb}_{11.5}\text{Ga}_{0.5}$ ($\Delta S_M = 13.5 \text{ J kg}^{-1} \text{ K}^{-1}$),³⁹ $\text{Ni}_{50}\text{Mn}_{38}\text{Sb}_{12}$ ($\Delta S_M = 12.1 \text{ J kg}^{-1} \text{ K}^{-1}$),⁴⁰ and $\text{Ni}_{43}\text{Mn}_{46}\text{Sn}_{11}$ ($\Delta S_M = 10.4 \text{ J kg}^{-1} \text{ K}^{-1}$)⁴¹ alloys.

The refrigeration capacity RC , which was analyzed for the ribbons, represents the amount of thermal energy that can be transferred by magnetic refrigerants between the cold (T_{cold}) and hot (T_{hot}) sinks in one ideal thermodynamic cycle. RC can be evaluated as $RC = \int_{T_{cold}}^{T_{hot}} \Delta S_M dT$, where T_{hot} and T_{cold} are the corresponding temperatures at the full width half maximum peak value of ΔS_M . Figure 8(d) illustrates the field dependence of the RC values for the $\text{Mn}_{50}\text{Ni}_{39}\text{In}_9\text{Co}_2$, $\text{Mn}_{50}\text{Ni}_{38}\text{In}_9\text{Co}_3$, and $\text{Mn}_{50}\text{Ni}_{37}\text{In}_9\text{Co}_4$ ribbons. The RC values show a near-linear increase with the magnetic field. Under the magnetic field change $\mu_0\Delta H$ of 5 T, the maximum RC for the $\text{Mn}_{50}\text{Ni}_{39}\text{In}_9\text{Co}_2$, $\text{Mn}_{50}\text{Ni}_{38}\text{In}_9\text{Co}_3$, and $\text{Mn}_{50}\text{Ni}_{37}\text{In}_9\text{Co}_4$ ribbons was determined as 110, 197, and 188 J kg^{-1} , respectively.

The RC values of the proposed material are comparable with those of the $\text{Ni}_{51.1}\text{Mn}_{31.2}\text{In}_{17.7}$ annealed ribbon ($RC = 195 \text{ J kg}^{-1}$, $\mu_0\Delta H = 5 \text{ T}$),⁴² and bulk $\text{Ni}_{50}\text{Mn}_{34}\text{In}_{16}$ ($RC = 180.8 \text{ J kg}^{-1}$, $\mu_0\Delta H = 5 \text{ T}$),⁴³ $\text{Ni}_{47}\text{Mn}_{40}\text{Sn}_{13}$ ($RC = 207 \text{ J kg}^{-1}$, $\mu_0\Delta H = 5 \text{ T}$),⁴⁴ and Ni_2MnIn ($RC = 167.5 \text{ J kg}^{-1}$, $\mu_0\Delta H = 5 \text{ T}$)⁴⁵ alloys. Moreover, the presented RC values are better than those of the bulk $\text{Ni}_{50}\text{Mn}_{34}\text{Sn}_8\text{In}_8$ ($RC = 47 \text{ J kg}^{-1}$, $\mu_0\Delta H = 5 \text{ T}$),⁴⁶ $\text{Ni}_{50}\text{Mn}_{35}\text{In}_{13.9}\text{B}_{1.1}$ ($RC = 140 \text{ J kg}^{-1}$, $\mu_0\Delta H = 5 \text{ T}$),⁴⁷ $\text{Ni}_{50}\text{Mn}_{37}\text{Sn}_{13}$ ($RC = 75 \text{ J kg}^{-1}$, $\mu_0\Delta H = 5 \text{ T}$),⁴⁸ $\text{Ni}_{45}\text{Co}_{6.4}\text{Mn}_{37}\text{In}_{11.6}$ ($RC = 95 \text{ J kg}^{-1}$, $\mu_0\Delta H = 5 \text{ T}$),⁴⁹ and $\text{Ni}_{50}\text{Mn}_{37}\text{Sb}_{13}$ ($RC = 37.7 \text{ J kg}^{-1}$, $\mu_0\Delta H = 5 \text{ T}$)⁵⁰ alloys as well as the $\text{Ni}_{52}\text{Mn}_{26}\text{Ga}_{22}$ ribbon ($RC = 70 \text{ J kg}^{-1}$, $\mu_0\Delta H = 5 \text{ T}$).²⁵

Figure 9 shows the field dependence of the temperatures T_{hot} and T_{cold} , which represent the full width at half maximum (δT_{FWHM}) of the ΔS_M curves for the $\text{Mn}_{50}\text{Ni}_{39}\text{In}_9\text{Co}_2$, $\text{Mn}_{50}\text{Ni}_{38}\text{In}_9\text{Co}_3$, and $\text{Mn}_{50}\text{Ni}_{37}\text{In}_9\text{Co}_4$ ribbons. The operational temperature range of the refrigerators δT_{FWHM} is determined based on T_{hot} and T_{cold} as $\delta T_{FWHM} = T_{hot} - T_{cold}$. It is seen in Fig. 9 that the magnetic field-induced inverse martensitic transformation causes δT_{FWHM} to gradually widen for larger magnetic fields. In particular, under a field change of 5 T, a large δT_{FWHM} up to 31 K

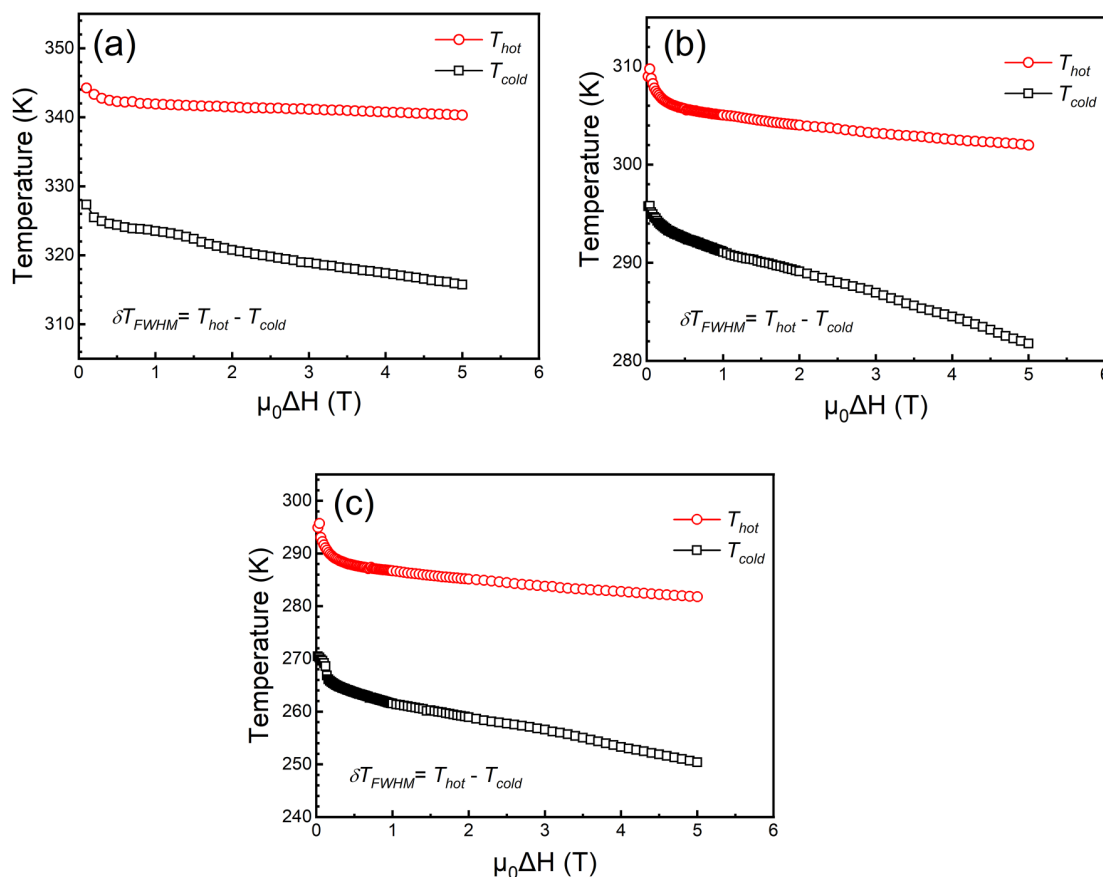


FIG. 9. Field dependence for temperatures T_{hot} and T_{cold} of the melt-spun ribbons: (a) $\text{Mn}_{50}\text{Ni}_{39}\text{In}_9\text{Co}_2$, (b) $\text{Mn}_{50}\text{Ni}_{38}\text{In}_9\text{Co}_3$, and (c) $\text{Mn}_{50}\text{Ni}_{37}\text{In}_9\text{Co}_4$.

TABLE II. Magnetocaloric properties of the $\text{Mn}_{50}\text{Ni}_{41-x}\text{In}_9\text{Co}_x$ ($2 \leq x \leq 4$) ribbons under a field change of 5 T.

Ribbon	ΔS_M ($\text{J K}^{-1} \text{kg}^{-1}$)	RC (J kg^{-1})	δT_{FWHM} (K)	T_{hot} (K)	T_{cold} (K)
$\text{Mn}_{50}\text{Ni}_{39}\text{In}_9\text{Co}_2$	5.7	110	24	340	316
$\text{Mn}_{50}\text{Ni}_{38}\text{In}_9\text{Co}_3$	12.1	197	20	302	282
$\text{Mn}_{50}\text{Ni}_{37}\text{In}_9\text{Co}_4$	7.5	188	32	282	251

was achieved for the $\text{Mn}_{50}\text{Ni}_{37}\text{In}_9\text{Co}_4$ ribbon, which is attributed to the relatively higher magnetic field-induced reduction rate of the transformation temperature of 7.4 K T^{-1} . The δT_{FWHM} is comparable to that in the bulk $\text{Ni}_{40}\text{Co}_{10}\text{Mn}_{40}\text{Sn}_{10}$ alloy ($\delta T_{FWHM} = 33 \text{ K}$, $\mu_0\Delta H = 5 \text{ T}$).⁴³ Moreover, the presented δT_{FWHM} is also larger than those in bulk $\text{Ni}_{41}\text{Co}_7\text{Fe}_2\text{Mn}_{40}\text{Sn}_{10}$ ($\delta T_{FWHM} = 20 \text{ K}$, $\mu_0\Delta H = 5 \text{ T}$),⁵¹ $\text{Ni}_{41}\text{Co}_{6.5}\text{Fe}_{2.5}\text{Mn}_{40}\text{Sn}_{10}$ ($\delta T_{FWHM} = 22 \text{ K}$, $\mu_0\Delta H = 5 \text{ T}$),⁵¹ $\text{Ni}_{40}\text{Co}_8\text{Mn}_{42}\text{Sn}_{10}$ ($\delta T_{FWHM} = 25 \text{ K}$, $\mu_0\Delta H = 5 \text{ T}$),²⁸ $\text{Ni}_{45}\text{Co}_5\text{Mn}_{36.6}\text{In}_{13.4}$ ($\delta T_{FWHM} = 20 \text{ K}$, $\mu_0\Delta H = 5 \text{ T}$),⁵² $\text{Ni}_{49.6}\text{Mn}_{38.4}\text{Sb}_{11.7}\text{Si}_{0.9}$ ($\delta T_{FWHM} = 7 \text{ K}$, $\mu_0\Delta H = 5 \text{ T}$),⁵³ $\text{Ni}_{45}\text{Co}_5\text{Mn}_{37}\text{In}_{13}$ ($\delta T_{FWHM} = 15.2 \text{ K}$, $\mu_0\Delta H = 5 \text{ T}$),⁵⁴ and $\text{Ni}_{45}\text{Co}_5\text{Mn}_{37}\text{In}_{12}\text{Si}_1$ ($\delta T_{FWHM} = 8.2 \text{ K}$, $\mu_0\Delta H = 5 \text{ T}$)⁵⁴ alloys. The magnetocaloric properties under a field change of 5 T for the presented ribbons are summarized in Table II. In addition, as the operational temperature regions for the $\text{Mn}_{50}\text{Ni}_{39}\text{In}_9\text{Co}_2$, $\text{Mn}_{50}\text{Ni}_{38}\text{In}_9\text{Co}_3$, and $\text{Mn}_{50}\text{Ni}_{37}\text{In}_9\text{Co}_4$ ribbons are adjacent, indicating the refrigeration temperature region can be further extended by forming a composite material with these ribbons.

IV. CONCLUSIONS

The magnetostructural transformation and magnetocaloric properties of Mn-rich $\text{Mn}_{50}\text{Ni}_{41-x}\text{In}_9\text{Co}_x$ melt-spun ribbons were investigated. It is demonstrated that the large temperature gradient during the melt-spinning process causes the initial austenite to form typical columnar-shaped grains with strong $\langle 001 \rangle_A$ preferred orientations perpendicular to the ribbon plane. The ribbons undergo a martensitic transformation from cubic austenite to monoclinic 8 M martensite. The 8 M martensite has a plate shape and is characterized by stacking faults as the internal structure. The STEM observations indicate that the lattice modulation of 8 M martensite is inhomogeneous at the atomic scale. The introduction of Co not only results in a gradual decrease of the martensitic transformation temperature but also converts the martensitic transformation from paramagnetic into meta-magnetic. The large magnetization difference ΔM associated with martensitic transformation gives large ΔS_M values of 5.7, 12.1, and $7.5 \text{ J kg}^{-1} \text{ K}^{-1}$ and RC values up to 110, 197, and 188 J kg^{-1} under a field change of 5 T for the $\text{Mn}_{50}\text{Ni}_{39}\text{In}_9\text{Co}_2$, $\text{Mn}_{50}\text{Ni}_{38}\text{In}_9\text{Co}_3$, and $\text{Mn}_{50}\text{Ni}_{37}\text{In}_9\text{Co}_4$ ribbons, respectively. Moreover, the enhanced magnetic field-induced reduction rate of transformation temperature of 7.4 K T^{-1} provides for a wide operational temperature region of 31 K for the $\text{Mn}_{50}\text{Ni}_{37}\text{In}_9\text{Co}_4$ ribbon.

ACKNOWLEDGMENTS

This work was supported by the National Natural Science Foundation of China (NNSFC; Grant Nos. 51771048 and

51431005), the Fundamental Research Funds for the Central Universities of China (Grant No. N180204013), the Liaoning Revitalization Talents Program (Grant Nos. XLYC1907082 and XLYC1802023), the 111 Project of China 2.0 (No. BP0719037), and CONACYT-SEP of Mexico (No. A1-S-37066). J. L. Sánchez Llamazares acknowledges the support received from Laboratorio Nacional de Investigaciones en Nanociencias y Nanotecnología (LINAN, IPICYT) to develop this work. C. F. Sánchez-Valdés is grateful to DMCU-UACJ for supporting his research stays at IPICYT (program PFCE and academic mobility grant).

DATA AVAILABILITY

The data that support the findings of this study are available from the corresponding author upon reasonable request.

REFERENCES

- Y. Sutou, Y. Imano, N. Koeda, T. Omori, R. Kainuma, K. Ishida, and K. Oikawa, *Appl. Phys. Lett.* **85**, 4358–4360 (2004).
- R. Kainuma, Y. Imano, W. Ito, Y. Sutou, H. Morito, S. Okamoto, O. Kitakami, K. Oikawa, A. Fujita, T. Kanomata, and K. Ishida, *Nature* **439**, 957–960 (2006).
- J. A. Monroe, I. Karaman, B. Basaran, W. Ito, R. Y. Umetsu, R. Kainuma, K. Koyama, and Y. I. Chumlyakov, *Acta Mater.* **60**, 6883–6891 (2012).
- R. Kainuma, Y. Imano, W. Ito, H. Morito, Y. Sutou, K. Oikawa, A. Fujita, K. Ishida, S. Okamoto, O. Kitakami, and T. Kanomata, *Appl. Phys. Lett.* **88**, 192513 (2006).
- H. E. Karaca, I. Karaman, B. Basaran, Y. Ren, Y. I. Chumlyakov, and H. J. Maier, *Adv. Funct. Mater.* **19**, 983–998 (2009).
- Z. Li, K. Xu, H. M. Yang, Y. L. Zhang, and C. Jing, *J. Appl. Phys.* **117**, 223904 (2015).
- S. Y. Yu, L. Ma, G. D. Liu, Z. H. Liu, and X. X. Zhang, *Appl. Phys. Lett.* **90**, 242501 (2007).
- D. Bourgault, T. Jérémy, P. Courtois, D. Maillard, and X. Chaud, *Appl. Phys. Lett.* **96**, 132501 (2010).
- Z. B. Li, W. Hu, F. H. Chen, M. G. Zhang, Z. Z. Li, B. Yang, X. Zhao, and L. Zuo, *J. Magn. Magn. Mater.* **452**, 249–252 (2018).
- J. Liu, T. Gottschall, K. P. Skokov, J. D. Moore, and O. Gutflisch, *Nat. Mater.* **11**, 620–626 (2012).
- Z. B. Li, Y. W. Jiang, Z. Z. Li, C. F. Sánchez-Valdés, J. L. Sánchez Llamazares, B. Yang, Y. D. Zhang, C. Esling, X. Zhao, and L. Zuo, *IUCr* **5**, 54–66 (2018).
- Z. Z. Li, Z. B. Li, B. Yang, X. Zhao, and L. Zuo, *Scr. Mater.* **151**, 61–65 (2018).
- D. Y. Cong, L. Huang, V. Hardy, D. Bourgault, X. M. Sun, Z. H. Nie, M. G. Wang, Y. Ren, P. Entel, and Y. D. Wang, *Acta Mater.* **146**, 142–151 (2018).
- Z. B. Li, J. J. Yang, D. Li, Z. Z. Li, B. Yang, H. L. Yan, C. F. Sánchez-Valdés, J. L. Sánchez Llamazares, Y. D. Zhang, C. Esling, X. Zhao, and L. Zuo, *Adv. Electron. Mater.* **5**, 1800845 (2019).
- Z. Z. Li, Z. B. Li, D. Li, J. J. Yang, B. Yang, Y. Hu, D. H. Wang, Y. D. Zhang, C. Esling, X. Zhao, and L. Zuo, *Acta Mater.* **192**, 52–59 (2020).
- Y. H. Qu, D. Y. Cong, X. M. Sun, Z. H. Nie, W. Y. Gui, R. G. Li, Y. Ren, and Y. D. Wang, *Acta Mater.* **134**, 236–248 (2017).
- L. Ma, S. Q. Wang, Y. Z. Li, C. M. Zhen, D. L. Hou, W. H. Wang, J. L. Chen, and G. H. Wu, *J. Appl. Phys.* **112**, 083902 (2012).
- H. C. Xuan, S. C. Ma, Q. Q. Cao, D. H. Wang, and Y. W. Du, *J. Alloys Compd.* **509**, 5761–5764 (2011).
- J. Ren, H. W. Li, S. T. Feng, Q. J. Zhai, J. X. Fu, Z. P. Luo, and H. X. Zheng, *Intermetallics* **65**, 10–14 (2015).
- A. Ghosh and K. Mandal, *J. Phys. D Appl. Phys.* **46**, 435001 (2013).
- Y. W. Jiang, Z. B. Li, Z. Z. Li, Y. Q. Yang, B. Yang, Y. D. Zhang, C. Esling, X. Zhao, and L. Zuo, *Eur. Phys. J. Plus* **132**, 42 (2017).
- B. Hernandez, J. L. Sánchez Llamazares, V. M. Prida, D. Baldomir, D. Serantes, M. Ilyn, and J. González, *Appl. Phys. Lett.* **94**, 222502 (2009).

- ²³Z. Wu, Z. Liu, H. Yang, Y. Liu, and G. Wu, *Appl. Phys. Lett.* **98**, 061904 (2011).
- ²⁴J. L. Sánchez Llamazares, T. Sanchez, J. D. Santos, M. J. Pérez, M. L. Sanchez, B. Hernando, L. Escoda, J. J. Suñol, and R. Varga, *Appl. Phys. Lett.* **920**, 012513 (2008).
- ²⁵Z. B. Li, Y. D. Zhang, C. F. Sanchez-Valdes, J. L. Sanchez Llamazares, C. Esling, X. Zhao, and L. Zuo, *Appl. Phys. Lett.* **104**, 044101 (2014).
- ²⁶Z. B. Li, N. F. Zou, C. F. Sánchez-Valdés, J. L. Sánchez Llamazares, B. Yang, Y. Hu, Y. D. Zhang, C. Esling, X. Zhao, and L. Zuo, *J. Phys. D Appl. Phys.* **49**, 025002 (2016).
- ²⁷D. Y. Cong, S. Roth, and L. Schultz, *Acta Mater.* **60**, 5335–5351 (2012).
- ²⁸Z. B. Li, Z. Z. Li, J. J. Yang, B. Yang, X. Zhao, and L. Zuo, *Intermetallics* **100**, 57–62 (2018).
- ²⁹Y. Q. Yang, Z. B. Li, Z. Z. Li, J. J. Yang, B. Yang, H. L. Yan, Y. D. Zhang, C. Esling, X. Zhao, and L. Zuo, *Crystals* **7**, 289 (2017).
- ³⁰Z. B. Li, J. L. Sánchez Llamazares, C. F. Sánchez-Valdés, Y. D. Zhang, C. Esling, X. Zhao, and L. Zuo, *Appl. Phys. Lett.* **100**, 174102 (2012).
- ³¹Z. B. Li, B. Yang, N. F. Zou, Y. D. Zhang, C. Esling, W. M. Gan, X. Zhao, and L. Zuo, *Materials* **10**, 463 (2017).
- ³²Z. B. Li, B. Yang, Y. D. Zhang, C. Esling, N. F. Zou, X. Zhao, and L. Zuo, *Acta Mater.* **74**, 9–17 (2014).
- ³³Z. B. Li, Y. D. Zhang, C. Esling, X. Zhao, and L. Zuo, *Acta Mater.* **59**, 2762–2772 (2011).
- ³⁴J. Sharma and K. G. Suresh, *J. Alloys Compd.* **620**, 329–336 (2015).
- ³⁵A. K. Pathak, M. Khan, I. Dubenko, S. Stadler, and N. Ali, *Appl. Phys. Lett.* **90**, 262504 (2007).
- ³⁶Z. H. Liu, S. Aksoy, and M. Acet, *J. Appl. Phys.* **105**, 033913 (2009).
- ³⁷S. Pandey, A. Quetz, I. D. Rodionov, A. Aryal, M. I. Blinov, I. S. Titov, V. N. Prudnikov, A. B. Granovsky, I. Dubenko, S. Stadler, and N. Ali, *J. Appl. Phys.* **117**, 183905 (2015).
- ³⁸L. Huang, D. Y. Cong, L. Ma, Z. H. Nie, Z. L. Wang, H. L. Suo, Y. Ren, and Y. D. Wang, *Appl. Phys. Lett.* **108**, 032405 (2016).
- ³⁹R. Sahoo, A. K. Nayak, K. G. Suresh, and A. K. Nigam, *J. Appl. Phys.* **109**, 07A921 (2011).
- ⁴⁰W. J. Feng, J. Du, B. Li, W. J. Hu, Z. D. Zhang, X. H. Li, and Y. F. Deng, *J. Phys. D Appl. Phys.* **42**, 125003 (2009).
- ⁴¹Z. D. Han, D. H. Wang, C. L. Zhang, H. C. Xuan, J. R. Zhang, B. X. Gu, and Y. W. Du, *Mater. Sci. Eng. A* **157**, 40–43 (2009).
- ⁴²J. L. Sánchez Llamazares, H. Flores-Zuñiga, C. Sánchez-Valdes, C. A. Ross, and C. García, *J. Appl. Phys.* **111**, 07A932 (2012).
- ⁴³V. K. Sharma, M. K. Chattopadhyay, and S. B. Roy, *J. Phys. D Appl. Phys.* **40**, 1869–1873 (2007).
- ⁴⁴A. G. Varzaneh, P. Kameli, T. Amiri, K. K. Ramachandran, A. Mar, I. A. Sarsari, J. L. Luo, T. H. Etsell, and H. Salamati, *J. Alloys Compd.* **708**, 34–42 (2017).
- ⁴⁵J. Brock and M. Khan, *J. Magn. Magn. Mater.* **425**, 1–5 (2017).
- ⁴⁶S. Dwevedi and B. Tiwari, *J. Alloys Compd.* **540**, 16–20 (2012).
- ⁴⁷S. Pandey, A. Quetz, A. Aryal, I. Dubenko, D. Mazumdar, S. Stadler, and N. Ali, *J. Magn. Magn. Mater.* **444**, 98–101 (2017).
- ⁴⁸T. L. Phan, P. Zhang, N. H. Dan, N. H. Yen, P. T. Thanh, T. D. Thanh, M. H. Phan, and S. C. Yu, *Appl. Phys. Lett.* **101**, 212403 (2012).
- ⁴⁹F. Chen, J. L. Sánchez Llamazares, C. F. Sánchez-Valdés, P. Müllner, Y. X. Tong, and L. Li, *Shap. Mem. Superelasticity* **6**, 54–60 (2020).
- ⁵⁰J. Du, Q. Zheng, W. J. Ren, W. J. Feng, X. G. Liu, and Z. D. Zhang, *J. Appl. Phys. D Appl. Phys.* **40**, 5523–5526 (2007).
- ⁵¹F. Chen, J. L. Sánchez Llamazares, C. F. Sánchez-Valdés, F. H. Chen, Z. B. Li, Y. X. Tong, and L. Li, *J. Alloys Compd.* **825**, 154053 (2020).
- ⁵²L. Chen, F. X. Hu, J. Wang, L. F. Bao, J. R. Sun, B. G. Shen, J. H. Yin, and L. Q. Pan, *Appl. Phys. Lett.* **101**, 012401 (2012).
- ⁵³R. Zhang, M. Qian, X. Zhang, F. Qin, L. Wei, D. Xing, X. Cui, J. Sun, L. Geng, and H. Peng, *J. Magn. Magn. Mater.* **428**, 464–468 (2017).
- ⁵⁴Z. B. Li, S. Y. Dong, Z. Z. Li, B. Yang, F. Liu, C. F. Sánchez-Valdés, J. L. Sánchez Llamazares, Y. D. Zhang, C. Esling, X. Zhao, and L. Zuo, *Scr. Mater.* **159**, 113–118 (2019).